JET-P(95)10

A Visible and UV Charge Exchange Spectroscopy System for the Tritium Phase of JET

H W Morsi[1], M von Hellermann, R W T König, H Schröpf[2].

JET Joint Undertaking, Abingdon, Oxfordshire, OX14 3EA, UK.
[1] Commission of the European Communities, DGXII, Brussels, Belgium.
[2] Siemens-Forschungslabor, Erlangen, Germany.

Preprint of a paper to be submitted for publication in
Plasma Physics and Controlled Fusion

April 1995

ABSTRACT

Results achieved by a direct optical link between torus and remote instruments designed for the active phase of JET are reported. The system is based on a labyrinth light path and a set of remotely controllable relay mirrors avoiding a direct view of the plasma core thus reducing the number of neutrons scattered into the detection path. Similar labyrinth systems are presently discussed for next-step fusion experiments with appreciable radiation levels inhibiting the use of fibres in the immediate neighbourhood of the torus. The JET mirror-link covers a spectral range from 2000 to 8000Å which extends considerably the range accessible by standard fibre-links.

The suitability of dominant UV charge exchange spectra for routine ion temperature and ion density diagnostics is addressed by comparing UV and visible CX spectra of CVI, BeIV, HeII and NeX which represent the main light impurities in a JET plasma. As a general rule it is found that the gain in the increase of atomic emission cross-sections for UV CX lines compared to their twins in the visible range is offset by the presence and intensity of additional edge emission lines in the same spectral neighbourhood. The exception of this rule is the UV CX spectrum of BeIV at 2530Å which is characterised by only a few background spectral lines and which offers a straightforward spectral analysis. In the case of the intense, but complex, CVI UV spectrum at 3434Å atomic modelling of line ratios has led to a successful reduction of free parameters and to the extraction of ion temperature values consistent with independent measurements.

1. INTRODUCTION

Optical fibres, which are used in present fusion devices as standard link between plasma experiment and remote spectral instruments located beyond a biological shield, will be subject to much enhanced radiation levels in full d-t phase operations, Ramsay et al.(1992), Morgan(1992). Two alternative solutions are currently taken into consideration for next-step fusion devices. One is the use of heated quartz fibres in the immediate neighbourhood of the machine, which are kept at temperatures above 300 °C, and which promise a reduction of neutron induced transmission losses. The second alternative, which is described in this paper, is a direct, fibre-less optical link with a labyrinth light path in between plasma and spectrometers avoiding a direct view of neutrons escaping the plasma. Some results of the JET direct link system achieved during its commissioning phase were reported in an earlier conference contribution, Morsi et al.(1991) and a first summary of the evaluation of UV CX spectra was given in Schröpf(1992). In the present paper an overview is given of results following an analysis of the last JET experimental campaign.

In contrast to standard fibre-links a mirror-link, with its many components, requires an appreciable effort in its design and a high degree of the overall mechanical stability. This is in particular the case for the JET tokamak, where the vessel movement caused by thermal expansion - the vessel is kept at 350°C - is of the order of 35 mm, and needs an active alignment and control system. Moreover, the light has to be transferred over a distance of 30m. A similar active alignment system had been developed in the past for the JET LIDAR diagnostic, Salzmann et al.(1989). The optical system described in this paper has a similar two-fold light path used for a simultaneous collection of plasma light and a concentric outer alignment channel transferring laser light between individual retro-reflectors located along the optical link and position sensitive detector arrays close to the spectrometer site.

A further field that is addressed in this paper is the extension of accessible transitions for active charge exchange spectroscopy, von Hellermann et al.(1993), Summers et al.(1993). In theory, lower quantum shell number transitions promise higher emission rates, and UV transitions should therefore be more advantageous than transitions in the visible wavelength range (cf. table I). For example, the visible CX transitions CVI(n=8→n=7, =5290.5Å), BeIV(n=7→n=6, =4658.5Å) and HeII(n=4→n=3, =4685.3Å), which are used as routine plasma diagnostic tools for the measurement of ion temperatures, plasma rotation and ion densities, have emission rates which are a factor two to three lower than corresponding transitions in the UV range.

In contrast to visible CX transitions, which have been tested extensively in the past, von Hellermann et al.(1992), only sparse data exist on the use of UV CX transitions for quantitative spectroscopy. The suitability for plasma diagnosis has to be proven by comprehensive consistency checks. This includes comparisons with temperatures of other low-Z ions or complementary ion temperature diagnostic, for example, high-Z ion temperatures derived from passive x-ray spectroscopy. An additional, entirely independent check is the validity of ion densities derived from the intensity of a CX spectrum. Global plasma effective ion charges deduced from CX results must be consistent with values deduced from the measurement of continuum radiation. Or in the exceptional case of a pure helium discharge the derived helium ion density must be half the electron density. Finally the prediction of thermal-thermal neutron rates is a highly sensitive function of ion temperature values, and must be consistent both with results from neutron diagnostics and plasma prediction codes.

The deduction of ion temperature values from active CX spectra depends crucially on the unique separation of locally well defined CX features and passive, non-localised emission spectra radiated close to the plasma boundary. The unique identification of the passive background spectrum is therefore a crucial step in the evaluation of UV CX spectrum. The observation of the intense UV CVI (n=7→n=6) spectrum at 3434Å has been reported in early papers on charge exchange spectroscopy (c.f. Carolan et al. (1987)). The fact that it is not used

in any of the present main fusion devices as a routine CX line may be partly explained by the actual complexity of its spectral structure which rules-out a straightforward single-component analysis. In this paper an attempt is made to investigate more details of the spectral components, and to model the excitation processes involved in its passive and active line emissions. The extracted ion temperature values are compared with independent ion temperature diagnostics at JET, that is, other CX instruments monitoring either the spectra of CVI or that of other low-Z impurities.

2. INSTRUMENTATION

An essential feature of the direct optical link, with regard to the tritium phase of JET, is a labyrinth optical system consisting of four mirrors, avoiding a direct view of the tokamak and thus minimising the neutron flux at the location of the spectrometers. The first mirror (A) (Fig.1) on top of the observation port reflects the light sideways towards mirror (B) mounted onto a limb of the iron transformer core. A flat mirror (C) at the outer end of a narrow penetration through the ceiling of torus hall is located beyond the biological shield. The diameter of the penetration tube (95mm) which is defined by the accepted level of neutrons expected to reach via multiple scattering processes the roof laboratory determines effectively the maximum étendue of the optical system. Mirrors A and B are assemblies consisting each of a spherical inner part for the plasma light and two flat outer parts used by an automatic mirror alignment system. The spherical shape of the inner part is preferred over a cylindrical shape to avoid alignment problems between inner and outer mirror sections.

The fourth mirror (D) is entirely spherical and focuses the plasma light via a beam splitter onto two Czerny-Turner spectrometers equipped with multi-channel plate intensifiers and linear array detectors. Only one of the two spectrometers was used in the 1991 experimental described in this paper.

The critical feature of the system is the alignment stability of its mirrors caused by the combination of long light paths with small apertures. The limiting components in the optical link are the narrow penetration between torus hall and roof laboratory and also the small entrance port on top of the torus. For this reason mirror (B) is used as field mirror (field lens). The f-number of the direct optical link is matched to the spectrometer (f/D = 8.7) and ray tracing confirms that 95% of rays emanating from an area of $2.5 \times 0.25 mm^2$ at the spectrometer entrance slit reach the torus mid-plane. The mirrors are coated with UV-enhanced aluminum permitting spectroscopic access down to the atmospheric cut-off wavelength of around 200nm. An evaluation of the overall sensitivity and a comparison of absolute calibration factors gained at the top of the torus with those gained directly in front of the spectrometer revealed that the penalty of the broad band coating is shown by the reflection coefficient which

was found to be only of the order 75% for each of the mirrors leading to a total loss factor introduced by the four mirrors of about 3.2.

For the commissioning phase of the optical link a beam splitter cube was introduced in between port window and mirror (A) enabling the coupling of a standard optical head plus fibre to the same viewing port. The same beam splitter is used for the coupling of an absolutely calibrated light source (LICOR 9L1800-02) into the optical path. The optical properties of the port window and of the beam splitter are measured separately.

An overview of the system components in the roof laboratory is given in Fig.2. The alignment system is outlined in Fig.3. Mirror H is inserted at an angle of 45° into the light path between mirrors C and D and consists of an elliptical hole in a flat surface, with major axes of 84.9mm and 60mm. This allows the penetration of a plasma light beam of circular shape and 60mm in diameter, while reflecting the alignment laser light and its return from retro-reflectors near the mirrors A, B, C (Fig.4). The light returned by the retro-reflectors is imaged as dots onto 2-dim position sensitive diode detectors installed on the optical bench of the alignment system (Fig.3), two for each mirror. Tilting a mirror results in movement of corresponding two light dots across the 2-dim diodes. The mirror must be adjusted in sequence, starting with the mirror nearest to the alignment bench, i.e. mirror C. For each spectrum taken by the cameras, a complete set of dot positions, and additionally the coarse regular positions of the axes of mirrors A, B, C measured by induction meters connected to the mirror mount axis, is recorded. Before the automatic alignment system can take over, the entire opto-mechanical system including the spectrometers and cameras have to be manually adjusted to the same optical axis. The common optical axis should end in the plasma volume intended for measurement (Fig.1), and is defined by a second alignment system permanently attached to the side exit of one spectrometer (Figs.4 and 5).

The laser light of this second system is coupled into the common light path via a flip mirror, and has three purposes: a) Definition of the optical axis of the entire system using entrance (S2) and exit (S1) slits of the spectrometer as a reference, and inserting ≈0.2mm pin hole in the centre of the entrance slit. b) Construction of a light bundle of identical or larger opening cone (f-number ≤ 8.7) to that of the plasma light bundle received by the cameras, to study vignetting effects. c) Direct illumination of the entrance slit (S2) adjusted to normal operational width (200mm) to facilitate the positioning of the absolute calibration lamp by imaging the slit down to the tokamak port. This manual alignment is carried out only once at the start of an experimental campaign, with the Torus vessel heated to operational temperature.

3. ABSOLUTE CALIBRATION AND SENSITIVITY

The absolute calibration of the mirror-link has highlighted several problems of a direct optical link compared with an optical fibre transfer system: The mirror link with its larger number of

optical components presents, in the *visible wavelength range,* a considerably higher loss-factor than a single fibre connection. The narrow labyrinth system, imposed by the required reduction of the neutron level, also implies a limitation of the system's étendue. In a fibre-link, higher étendue spectrometers can be used and the full aperture of a single fibre is rarely fully exploited. However, for any spectroscopic investigation of line emissions in the UV wavelength range, only a direct-optical-link provides enough optical throughput, and a fibre-link cannot be used for wavelength below 4000Å.

The tungsten lamp source used at JET for the absolute calibration of spectroscopic instruments in the visible wavelength range is limited to wavelengths above 3500Å. Most of the dominant CX UV lines described in this paper are below this wavelength limit. For this reason a cross-calibration technique was used which is based on the measurement of continuum radiation, and the plasma itself acting as a global calibration source. In addition to providing an absolute calibration for UV spectra this technique monitors also indirectly the mechanical stability of the mirror link in comparison to fibre-links whose optical heads can be rigidly mounted to the torus structure and observation ports.

The cross-calibration technique is based on the assumption that a line-of-sight averaged effective ion charge of a plasma represents a global quantity, which is determined by local values of impurity densities, electron densities and electron temperatures. Each of those quantities is a constant on a magnetic flux surface. Any line of sight integrated measurement of the contiuum radiation is then representative for a specific impact radius, that is, the minor radius perpendicular to the line of sight.

$$\int I_{cont} dl = B \cdot \int_{\rho_{imp}}^{1} d\rho \frac{ds}{d\rho} g_{ff}(T_e(\rho), \lambda, Z) \cdot Z_{eff}(\rho) \cdot n_e^2(\rho) \frac{1}{\lambda \cdot \sqrt{T_e(\rho)}} \qquad (1)$$

with the constant $B = \left[\frac{e^2}{4\pi\varepsilon_0}\right]^3 \frac{16}{3hc^3 m_e^2} \sqrt{\frac{\pi \cdot m_e}{6}}$ and g_{ff} the free-free Gaunt factor. Each point along the integration path ds is mapped onto its associated magnetic flux surface or normalised minor radius $\rho = r/a$. The line-of -sight averaged Z_{eff} value derived from continuum radiation:

$$< Z_{eff}(\rho_{imp}) >= \frac{\int_{\rho_{imp}}^{1} I_{cont}(\rho) \frac{ds}{d\rho} d\rho}{B \int_{\rho_{imp}}^{1} d\rho \frac{ds}{d\rho} \frac{n_e^2(\rho) \cdot g_{ff}(\lambda, \rho)}{\lambda \cdot \sqrt{T_e(\rho)}}} \qquad (2)$$

The free-free gaunt factor $g_{ff}(,T_e,Z)$ is in the visible wavelength range only a weakly dependent function of the wavelength, ion charge and electron temperature (cf. Fig.6 and references, Summers(1986), Mewe et al.(1986)). Comparison of two continuum radiation measurements, representing the same impact parameter and hence $<Z_{eff}>$, and taking out the radial dependence of the gaunt factor leads to an approximated ratio:

$$\frac{\Phi^{UV}_{Brems}(\lambda_{UV})}{\Phi^{vis}_{Brems}(\lambda_{vis})} = \frac{\int I_{cont}(\lambda_{UV})ds}{\int I_{cont}(\lambda_{vis})ds} \approx \frac{\lambda_{vis}\, g_{ff}(\lambda_{UV})}{\lambda_{UV}\, g_{ff}(\lambda_{vis})} \tag{3}$$

$$\Phi^{UV}_{CX} = \Phi^{UV,uncalibrated}_{CX} \cdot \frac{\Phi^{vis}_{brems}}{\Phi^{UV,uncalibrated}_{brems}} \cdot \frac{\lambda_{vis}\, g_{ff}(\lambda_{UV})}{\lambda_{UV}\, g_{ff}(\lambda_{vis})} \tag{4}$$

4. EXPERIMENTAL ASSESSMENT OF EMISSION RATES FROM UV AND VISIBLE CX SPECTRA

The simultaneous measurement of UV and visible CX spectra offers, at least in principle, the option of comparing ratios of effective emission rates with values predicted by atomic modelling. It is of particular interest to study experimental evidence on modelled redistributions following charge capture into the most likely quantum shell n_{max}, and the decay by which the n-distribution is described (cf.Summers(1993)).

$$\frac{\sigma_{cx}(n)}{\sigma_{cx}(n_{max})} = \left(\frac{n_{max}}{n}\right)^{\alpha(E)} \tag{5}$$

The evaluation of two CX spectra representing the same ion in the same plasma volume should lead to the same ion density. However, in a real plasma experiment, several beam energy components and, in the case of the JET experiments described in this paper, two types of neutral beams (40keV/amu and 70keV/amu) contribute to the observed spectra. The JET deuterium neutral beams at 40 keV/amu have a power mixture f_E, $f_{E/2}$, $f_{E/3}$ of 0.79, 0.17, and 0.09 for their full, half and third energy components respectively and 0.65, 0.24, 0.14 for the 70keV/amu beams.

Therefore the following results rely on ratios of beam-averaged emission rates based on the contribution of each beam energy component and on experimentally observed line-ratios. The local impurity density n_Z is calculated from the integrated spectral intensity:

$$\Phi_{cx}(\lambda) = \frac{\Phi(R)}{\sqrt{\pi}\cdot\lambda_d}\int d\lambda \cdot e^{-\frac{(\lambda-\lambda_0)^2}{\lambda_d^2}}$$
$$\Phi_{cx}(R) = \frac{1}{4\pi}\cdot n_z(R)\cdot \sum_{beam}\sum_{E_i} <\sigma v(E_i,n,l)>_{cx} \int ds\cdot n_b(E_i,s,R) \quad (6)$$

Where the local beam density n_b is determined by:

$$n_b(R,E) = n_b(0,E)\exp\left\{-\int dr\cdot \sum_z \sigma_{stop,z}(E)c_z(R)\right\} \quad (7)$$

with the vacuum particle density:

$$n_b(0,E) = \frac{P\cdot f_E}{E\cdot v_E\cdot A} \quad (8)$$

Here P denotes the total beam power, f_E its power fraction at beam energy E, v_E the beam particle velocity, and A the neutral beam cross-section area. The emission volume is defined by the intersection of the vertical line of sight and, in the JET case, a bundle of eight neutral (deuterium or helium) beams injected close to the equatorial mid-plane. Integration $ds(x,y,z)\approx dy$ along the vertical line of sight determines the geometric fraction of each neutral beam which contributes to the CX spectrum. The neutral beams are described by a local Gaussian intensity profile $n_b(x,y,z)$, where the z-coordinate is along the neutral beam axis, y is approximately in viewing line (vertical) direction and x in the horizontal mid-plane:

$$n_b(x,y,z) = n_b(R,E)\frac{1}{\pi\cdot w_x(z)\cdot w_y(z)}\cdot\exp\left\{-\frac{x^2}{w_x^2(z)}-\frac{y^2}{w_y^2(z)}\right\} \quad (9)$$

Each of the eight beams has different coordinates x, y and z with respect to the viewing line, and the widths w_x, w_y vary with the different beam energy of each beam. Integration dr along the neutral beam path is between plasma boundary and observation volume. Total beam-stopping cross-sections $\sigma_{stop,z}$ and local impurity concentrations $c_z=n_z/n_e$ are required for the calculation.

Equation (5) may be re-written:

$$\Phi_{cx,n\to n'} = \frac{1}{4\pi} n_z n_{b,ave} Q_{ave}^{n,n'} \quad (10)$$

with:

$$Q_{ave}^{n,n'} = \frac{\sum_n \sum_k n_{b,n}(E_{k,n}) < \sigma v(E_{k,n}) >}{\sum_n \sum_k n_{b,k}(E_{k,n})} \quad \text{and} \quad n_{b,ave} = \sum_n \sum_k n_b(E_{k,n}) \qquad (11)$$

Provided the two photon fluxes are cross-calibrated by their respective bremsstrahlung signals, as in described by equation (4) one can compare the two ratios R and R^* , which are defined by:

$$R(t) = \frac{\Phi_{cx,n\to n'}(t)}{\Phi_{cx,m\to m'}(t)} \quad \text{and} \quad R^*(t) = \frac{Q_{ave,n\to n'}(t)}{Q_{ave,m\to m'}(t)} \qquad (12)$$

For a significant neutral beam attenuation at minor radius r, (i.e. $\zeta_E(r) = \frac{n_b(r,E)}{n_b(a,E)} << 1$), which is the case for JET plasmas with electron densities close to $10^{20}m^{-3}$, the contributions of half and third energy components to effective values of R^* can be quite small (<10%) and observed ratios essentially represent the full energy component. Moreover, for full beam energies close to the maximum of emission rate, the fractional energies have a much reduced effective emission rate, i.e. $\frac{< \sigma v >_{n\to n',E/2}}{< \sigma v >_{n\to n',E}} << 1$.

A straightforward interpretation of experimental data is provided in the case when two CX transitions of the same ion are part of the same spectrum, and no bremsstrahlung cross-calibration is required. This is the case, for example, for the visible HeII/BeIV spectrum, where two transitions of BeIV at =4658.5Å and =4685.25Å respectively can be measured by a single instrument. Experimental evidence, for example, of the intensity ratio of the two beryllium lines v(BeIV(6→5)):v(BeIV(8→6))=5.2 (cf. Fonck et al. (1983)) has led to a revision of the model describing the redistribution following charge capture.

In the case of a helium neutral beam acting of a donor for the CX excitation, only a single energy component is present (as for example, JET pulse #27586 (Fig.15)), and R and R^* reflect directly the effective rates predicted by atomic modelling.

5. SPECTROSCOPIC RESULTS

An overview of a first assessment of UV charge exchange (CX) spectra of fully ionised light impurities, emitted at the plasma centre of the JET tokamak, is presented in the following section. The primary goal of the overview has been the identification of the main spectral components in each spectrum. The second aim was to develop procedures for the extraction of the active CX spectrum for the deduction of central ion temperature and ion density determined by the Doppler width and line intensity respectively. The reliability of deduced ion temperature values was assessed by a comparison with the results of other CX diagnostic systems, one

further central chord, and two multi-chord systems providing radial ion temperature profiles (von Hellermann et al.(1992)). In addition to CX results, ion temperature measurements based on high resolution X-ray spectroscopy and electron temperature values based on Thomson scattering and electron cyclotron emission were also used for comparisons. The latter is justified in the case of high density plasmas where electron and ion temperatures can be assumed to be approximately equal.

The active-phase optical-link was used in the majority of its commisssioning phase for the measurement of the visible CVI CX transition. Fig.7 gives an overview of central ion temperatures deduced from the CVI spectrum as measured by the direct-optical link (with its line of sight perpendicular to the magnetic field) and a comparison with results from the same spectrum but measured by a multi-fibre link, located in the torus mid-plane, providing a complete radial profile. A limited number of experiments was dedicated to the assessment of the suitability of UV CX transitions of CVI and BeIV representing the main light impurities in a JET plasma.

The following sections (and Table 2) give an overview of analysed UV CX impurity spectra including corresponding spectra of the same ion in the visible wavelength range. All CX spectra are composite spectra i.e. a superposition of a passive 'cold' component, emitted near the plasma edge, and an active CX 'hot' component emitted at the plasma centre. In contrast to the first feature the localisation of the second is well defined by the intersection of optical axis of the observation system and neutral beam(s). The passive edge component is itself a composition of two features representing impact excitation and low-energy CX excitation close to plasma boundary respectively. The passive CX feature is the result of the interaction of a low-energy, but high-density, neutral deuterium population close to the magnetic separatrix and fully stripped impurity ions. Ion temperatures deduced from this feature as high as 2 to 3 keV have been observed in JET plasmas, von Hellermann et al.(1993). The close neighbourhood of the vertical line-of-sight to the X-point and recycling area for most of the JET discharges enhances the local neutral density and therefore the strength of both of the passive plasma edge features.

In theory, there should not be any interference from narrow edge lines, which are clearly separated by their wavelength position from the actual CX spectrum. However, very intense edge lines, which exceed the CX line intensities by a substantial factor (e.g. > 10), imply that the wings of the edge lines may interfere with the actual CX features. It is quite possible that low-amplitude wings of the instrument function may play a role in this interference. The instrument functions are usually approximated by a sum of Gaussians in order to facilitate a deconvolution procedure. The sensitivity of the wings of the instrument function on high line intensities may also depend on the type of detector which could be affected by cross-talk between adjacent pixels.

A similar problem is caused by low-intensity passive lines located in the wings of a CX spectrum. In this case the intensity is too low to have a noticeable effect on the standard deviation of the least squares fit, but is nevertheless strong enough to affect the wings of the CX spectrum.

5.1 UV CX spectra of carbon

Examples of CX spectra of CVI during NBI are presented in Fig.8 and Fig.9 which give an overview of the multi-line structure of the spectral region close to the CVI (n=7→n=6) CX transition. Fig.9a shows the passive edge emission spectrum before start of neutral beam injection. Close to the CVI transition at =3434Å there is a further, considerably weaker, CVI line at =3438Å. The identification of this line with the CVI (n=11→n=8, =3438Å) CX transition appears to be conclusive for several reasons:

First, the same temperature value can be derived from three independent CVI edge emissions, that is the two UV CVI lines at 3434Å and 3438Å, and also its twin visible transition at 5290Å(n=8→n=7) (Fig.9c); second, during the neutral beam injection phase actually two lines are present at 3438Å, and the second, the broader component, changes its width in the course of the injection and plasma heating phase. The broader component at 3438Å is therefore most likely also an active, localised, CX spectrum emitted from the same volume as the main (n=7→n=6) CVI spectrum. The wavelength coincides with the CVI (11→8) transition. The expected emission rate for n=3 emission following charge capture is small compared to a n=1 transition; third, the average amplitude ratio (27:1) of the two CVI transitions appears to be approximately constant within the experimental uncertainties (Fig.11).

These observations indicate that the 3438Å line emission is indeed the CVI 11→8 transition, and that width, intensity and position of two CVI lines may be coupled. The coupling of temperatures values of passive and active components, and also the coupling of the respective wavelengths reduces the free parameters of a four-component spectrum to five parameters.

It is also noteworthy, that if all the three (UV and visible) CVI lines are pre-dominantly excited by a passive charge exchange process between a population of neutral hydrogen close to the plasma separatrix and C^{6+} ions, the respective intensity ratio reflects also the populations of excited neutral hydrogen in n=2 and n=3 levels, which are resonant levels with the n=7→n=6 and n=11→n=8 CVI transitions. Therefore, the assumption of a constant intensity ratio, appears to be justified in the case of two passive CVI edge line spectra.

In theory, the wavelength coincidence of an OVI line at 3438Å, might suggest the presence of an oxygen line. However, the temperature identification, and also the low oxygen content of a JET plasma following beryllium evaporation, make the presence of a OVI line unlikely.

Fig.10 demonstrates the results of deduced central ion temperatures based on a constrained parameter fit coupling the two UV CVI CX components as well as their respective passive edge features. The survey is taken from a range of JET pulses with high neutral beam power and high central ion temperatures. JET pulses with full neutral beam power imply, for the 1991 experimental campaign, the simultaneous operation of 40 and 65 keV/amu neutral beams. One pair of neutral beams, which were part of a bank of neutral beams operated at 40keV/amu was used for example for the fuelling of tritium in the preliminary tritium experiment at JET, as reported in 1991. Both energies contribute to the UV CX spectrum and therefore an average values of 27:1 (that is 38:1 and 23:1 for 40keV/amu and 70keV/amu respectively) applies for the two CX transitions. The effective contribution is determined by the beam attenuation and also geometrical weighting factors.

The comparison is made, in a temperature range between 5 and 25 keV, with CX spectra measured simultaneously, based either on complete radial profiles of ion temperatures derived from the visible CVI(8→7) transition or, sharing the same viewing port of the UV link, the results of the standard fibre-link connected to spectrometers tuned to the n=8→7 CVI transition. The fact that a common central ion temperature value may be derived from three entirely differently structured spectra justifies the introduction of coupled parameter values in the treatment of the UV CVI CX spectrum. The general agreement is within 10 to 15%. It must however be stated that in spite of the apparent modelling success, the total number of investigated CVI UV spectra is still minute compared with the experience gained with its twin in the visible range.

The CX transition CVI (9→7) at = 3138.6Å entirely over-shadowed by the several orders of magnitude stronger BeII resonance line at =3130.0Å. Any spectral analysis and extraction of a CX CVI feature at this wavelength is not possible.

5.2 UV CX spectra of beryllium

Of the three CX BeIV spectra observed in the UV wavelength range only the dominant n=1 transition at 2530.5Å is of use for an ion temperature diagnostic. For completeness the CX BeIV transitions (n=8→n=5) and (n=7→n=5) are shown in Fig.12. In both cases the passive edge line emission exceeds the active spectrum by far.

The most promising UV spectrum for routine quantitative analysis of plasma parameters is the (n=5→n=4) transition at =2530.5Å (Fig. 13). Its effective rate in the visible wavelength range is approximately a factor 2.6 greater than that of the main n=1 transition at 4658.5Å. However, the main difference is the comparatively clean background spectrum. There is a CIV multiplet at 2523.7Å, 2424.4Å and 2527.7Å respectively, a weak CII multiplet at 2538.98Å, 2540.39Å, 2540.88Å and another as yet, unidentified line at 2536Å. The evaluation of the UV CX BeIV spectrum in terms of ion temperatures and ion densities has been studied for plasma

conditions with a sufficient beryllium content (>1% of the electron density). This has enabled a direct comparison with results obtained from the CX BeIV transition in the visible wavelength range (Fig. 14).

The UV BeIV CX spectrum appears in fact to be an exceptional example where the visible CX spectrum is undoubtedly more complex than the main UV spectrum. The visible BeIV spectrum (=4658.5Å) has been treated successfully in the past as part of the HeII spectrum (=4685.25Å) , von Hellermann et al. (1993b), Summers et al.(1991). The results from a wide range of beryllium densities (between 0.5% and 10% of the electron density) have shown that the visible BeIV spectrum can only be accepted as a stand-alone *temperature* analysis if the beryllium content in the plasma exceeds 5% (n_{Be}/n_e>0.05). The second constraint in the analysis of the visible BeIV CX spectrum is the amplitude of the neighbouring CIII triplet at 4647Å. The range of accessible beryllium densities may be extended to considerable lower levels if there is a sufficient level of helium in the plasma, and the width of the BeIV spectrum may be coupled to that of the HeII spectrum. In this case the beryllium density may be recovered. The densities limits of the UV BeIV CX spectrum need still to be ascertained.

5.3 UV CX spectra of helium

In the case of the UV CX HeII spectrum with a n=2 transition (n=5→n=3, =3202.8Å) the relative role of the passive line spectra is even more striking. The example shown in Fig.15 represents the case of an almost pure helium plasma ($n_{He}/n_e \approx 0.5$) with optimal signal-to-noise ratio. This is illustrated by consistent ion temperatures deduced from the visible 4→3 and the UV 5→3 transition and also by the apparent agreement of predicted and observed emission rates (Fig.16). Standard plasmas with significantly lower helium concentrations of typically $n_{He}/n_e < 0.05$, exclude however the use of the UV 5→3 HeII CX spectrum for routine diagnostic applications.

CX HeII spectra in the visible wavelength range have been extensively studied in the past , cf. Korotkov et al.(1992). Similar to most of the known low-Z spectra, the passive emission spectrum shows clearly the existence of both an electron impact as well as a low-energy CX excited population close to the plasma boundary. In the case of HeII spectrum the two passive populations are distinguishable by their different Doppler widths. Typical values for the electron impact excited component are <50eV, and for the passive charge exchange component values between 200 and 2000 eV are found. The spectra around the CX transitions of HeII during NBI are presented in Fig.15. For the visible CX spectrum the wavelength coincidence of HeII(n=4→n=3) and BeIV(n=8→n=6) leads for JET plasmas with an appreciable amount of beryllium (>1%), to an additional spectral component which needs to be considered. In practice, however, the existence of an intense BeIV(n=6→5) spectrum in the immediate

neighbourhood enables the coupling of the intensities of the two BeIV transitions, which effectively removes additional free parameters in least-square fit to the total spectrum.

5.4 UV CX spectra of neon

A spectrum around of the UV CX line of NeX is presented in Fig.17a, showing a complex structure with several CII and CIII multiplets in the same spectral range (CII: 3868.87Å, 3870.67Å, 3873.06Å, 3874.66Å, 3876.05Å, 3876.41Å, 3876.66Å, 3878.03Å, 3879.64Å, 3880.58Å, 3883.82Å and CIII : 3883.82Å, 3885.94Å, 3889.14Å). The spectrum is observed during a neon gas puff experiment with typical Ne^{+10} concentrations of less than 0.5% of the electron density. The presence of the edge lines make an unambiguous analysis, particular at low concentrations, difficult. The spectrum appears therefore not to be a recommendable candidate for ion temperature deductions. By contrast, the visible transition n=11→n=10 at =5249Å (Fig.17b) appears to have a wider range of applicability with resolvable concentrations as low as 0.03%, since the spectral width of the visible NeX spectrum may be coupled to that of its neighbour the CVI CX spectrum at 5290.5Å.

5.5 UV CX spectra of oxygen

Due to the low oxygen content of present JET plasmas following the introduction of graphite or beryllium tiles respectively and also Be-evaporation onto wall and limiter surfaces, is the estimated oxygen concentration (deduced from the OVIII (10→9) at γ = 6068.8Å) typically of the order 0.1% or less. The low oxygen level and also the complex spectral structure of the spectral environment next to the UV CX transition OVIII (n=8→n=7) at γ = 2975.8Å (Fig. 12c) have not encouraged systematic studies of this UV n =1 transition, whose emission rate is a factor 6.25 above the frequently evaluated visible CX transition iat 6068Å.

6. SUMMARY AND CONCLUSIONS

The described active phase spectroscopic system with a fully remote controllable direct optical mirror link has proven to be a mechanically stable diagnostic for visible and ultraviolet light. Since it consists entirely of reflecting optics it promises to be compatible with the requirements of D-T operations with much enhanced neutron rates. The spectral range has been considerably extended beyond the range accessible by quartz fibre links. However, the direct imaging properties of the optical link imply in the visible wavelength range a lower overall optical throughput compared to high étendue fibre-links. Absolute calibrations were achieved by both in-situ measurements and cross-calibration check with standard continuum radiation diagnostics at the JET experiment. The broad-band reflection coatings of the multi-mirror link

intended to cover both visible and UV spectral lines appear to contribute to most of the transfer losses.

A first evaluation of CX spectra in the UV range has shown that UV CX spectra are in general more complex than corresponding lines in the visible range. The strongest UV CVI CX spectrum at =3434Å comprises two active and two passive components, representing the n=7→6 and n=11→8 transitions at =3434Å and 3438Å respectively. Atomic modelling of the CX emission rates and a coupled least-square fit technique have enabled the deduction of central ion temperatures in generally good agreement with simultaneously measured ion temperature values provided by other diagnostics. The UV NeX spectrum at 3886Å is difficult to analyse due to the presence of several CII and CIII lines. The exception of this general experience is the UV spectrum of BeIV at 2530Å which appears to be less complex than the strongest BeIV transition in the visible range. In summary, the UV CX spectra investigated in this paper appear not to be a true alternative to their visible twins, and may therefore not be considered for routine ion temperature diagnostics.

A systematic exploitation of several CX transitions measured simultaneously in the visible and UV range allows in theory a direct comparison of effective emission rates of the same ion, and therefore a comparison to theoretical modelling of the redistribution processes following charge capture. As shown in this paper the extraction of usable emission rate data from experimental CX line ratios is a difficult task due to the mixture of different energy species, attenuation factors and spectral uncertainties. however, the results presented here indicate that experimental data and theoretical predictions are close to predicted ratio for a wide range of quantum shells and energies.

10. ACKNOWLEDGMENTS

The authors, especially H.W. Morsi, would like to thank Per Nielsen for the use of his optical ray tracing software and kind advice on problems in optics. The authors are also indebted to the technical support and expertise of Bernard Viaccoz, John Ryan and Harry Clarke.

REFERENCES

[1] Ramsey A.T., Hill K.W., Rev. Sci. Instrum. **63,** 4735 (1992).

[2] Morgan P.D. , Proc. 17th Symposium on Fusion Technology, Rome, 722 (1992).

[3] H.W. Morsi, R. Hatzky, M.G. von Hellermann, W. Mandl, R.R. McKillen et al., Proc.18th EPS Conf. on Contr. Fusion and Plasma Heating, Berlin, **15C**(4),261 (1991).

[4] Schröpf P.D., MSc Thesis, 'Analysis of UV Charge Exchange Spectra at the JET Experiment', Technische Universität München, FRG, (1992).

[5] Salzmann H., Bundgaard J., Gadd A., Gowers C., Gusev V., Hansen K.B., Hirsch K., Nielsen P., Reed K., Schrödter C., Weisberg K., "The LIDAR Thomson Scattering Diagnostic on JET", JET-R(89)07 (1989)

[6] von Hellermann M.G., Summers H.P., 'Active Beam Spectroscopy at JET', in 'Atomic and Plasma Material Interaction Processes in Controlled Thermonuclear Fusion', R.K.Janev and H.W.Drawin Ed., Elsevier Publishing Co. (1993)135-164, and JET-P(93)34.

[7] Summers H.P. and von Hellermann M.G., in 'Atomic and Plasma Material Interaction Processes in Controlled Thermonuclear Fusion', R.K.Janev and H.W.Drawin Ed., Elsevier Publishing Co. (1993)87-117

[8] von Hellermann M.G., Summers H.P., Rev. Sci. Instr. **63,** 5132(1992)

[9] Carolan P.G. , Duval B.P., Field A.R. Phys.Rev. A**35**,3454(1987)

[10] Summers H.P., JET-P(86)06

[11] Mewe R., Lemen J.R. , van den Oord G.H.J., Astron. Astrophys. **65**,511(1986)

[12] von Hellermann M.G., Core W.G.F. , Frieling W.G.F., Horton L.D., Mandl W., Summers H.P. Plasma Phys.Contr.Fusion **35**,799(1993)

[13] W. Mandl, R. Wolf, M.G. von Hellermann, H.P. Summers, Plasma Physics and Contr. Fusion **35**, 1373(1993).

[14] Fonck R.J., Goldston R.J., Kaita R., Post D.E., Appl.Phys.Lett.**42**,239(1983)

[15] Korotkov A.A. et al., 19'th EPS Conf. on Contr. Fusion and Plasma Phys., Innsbruck 1992

[16] Summers H.P., Dickson W., Boileau A., Burke B.G., Denne-Hinnov B., Fritsch W., Giannella R., Hawkes N.C., von Hellermann M., Mandl W., Peacock N.J., Reid R., Stamp M.F., Thomas P.R. (1991) Plasma Phys.Contr.Fusion **34**,325

Table1 : Overview of effective emission rates

ion	transition ($n_i \rightarrow n_f$)	(Å)	$v(10^{-15}m^3/s)$ 40keV/amu	$v(10^{-15}m^3/s)$ 70 keV/amu
Carbon	6→5	2070.3	63.40	51.8
CVI	8→6	2082.0	6.04	7.26
	9→7	3138.6	2.78	3.89
	7→6	3433.7	25.10	24.40
	11→8	3438.0	0.65	1.19
	8→7	5290.5	9.89	11.6
Beryllium BeIV	5→4	2530.5		16.7
	7→5	2906.2	2.83	2.57
	6→5	4658.5	8.56	6.99
	8→6	4685.2	1.56	1.54
	7→6	7726.2	4.03	3.29
Helium	5→3	3202.8	1.56	0.78
HeII	4→3	4685.2	4.51	2.03
	6→4	6559.5	0.65	0.35
Neon	9→8	2777.9	66.5	98.90
NeX	12→10	2981.5	3.51	9.66
	13→11	3881.2	1.80	5.95
	10→9	3884.0	30.9	56.3
	11→10	5249.2	13.7	30.7
	12→11	6901.6	6.27	17.2
	13→12	8868.3	3.07	10.2
Oxygen	10→8	2530.6	4.66	9.60
OVIII	8→7	2975.8	50.20	63.20
	11→9	3487.9	2.12	5.47
	9→8	4340.7	20.40	32.20
	12→10	4658.7	1.03	3.28
	10→9	6068.5	8.05	16.30

* Effective rate coefficients for T_i = 5keV, $n_i = 2.5 \cdot 10^{19} m^{-3}$, Z_{eff} = 2.0 [9].

Table 2 : Overview of observed ratios of effective rate coefficients

ion	transitions	wavelengths	neutral beam	R(observed)	R^*(expected)lling
C^{5+}	v(7→6)/v(11→8)	3434Å/3438Å	D^0 @70keV/amu	22.2±3.8	27.5
C^{5+}	v(7→6)/v(11→8)	3434Å/3438Å	D^0 @37keV/amu	30.1±8.1	43.0
C^{5+}	v(7→6)/v(8→7)	3434Å/5290Å	D^0 @37keV/amu	2.2±0.2	2.6±0.10
Be^{3+}	v(5→4)/v(6→5)	2530Å/4658Å	D^0 @65keV/amu	2.1±0.3	3.0±0.10
He^+	v(5→3)/v(4→3)	3203Å/4685Å	He^0@23keV/amu	0.30±0.05	0.35±0.03
He^+	v(5→3)/v(4→3)	3203Å/4685Å	He^0@33keV/amu	0.38±0.05	0.37±0.03

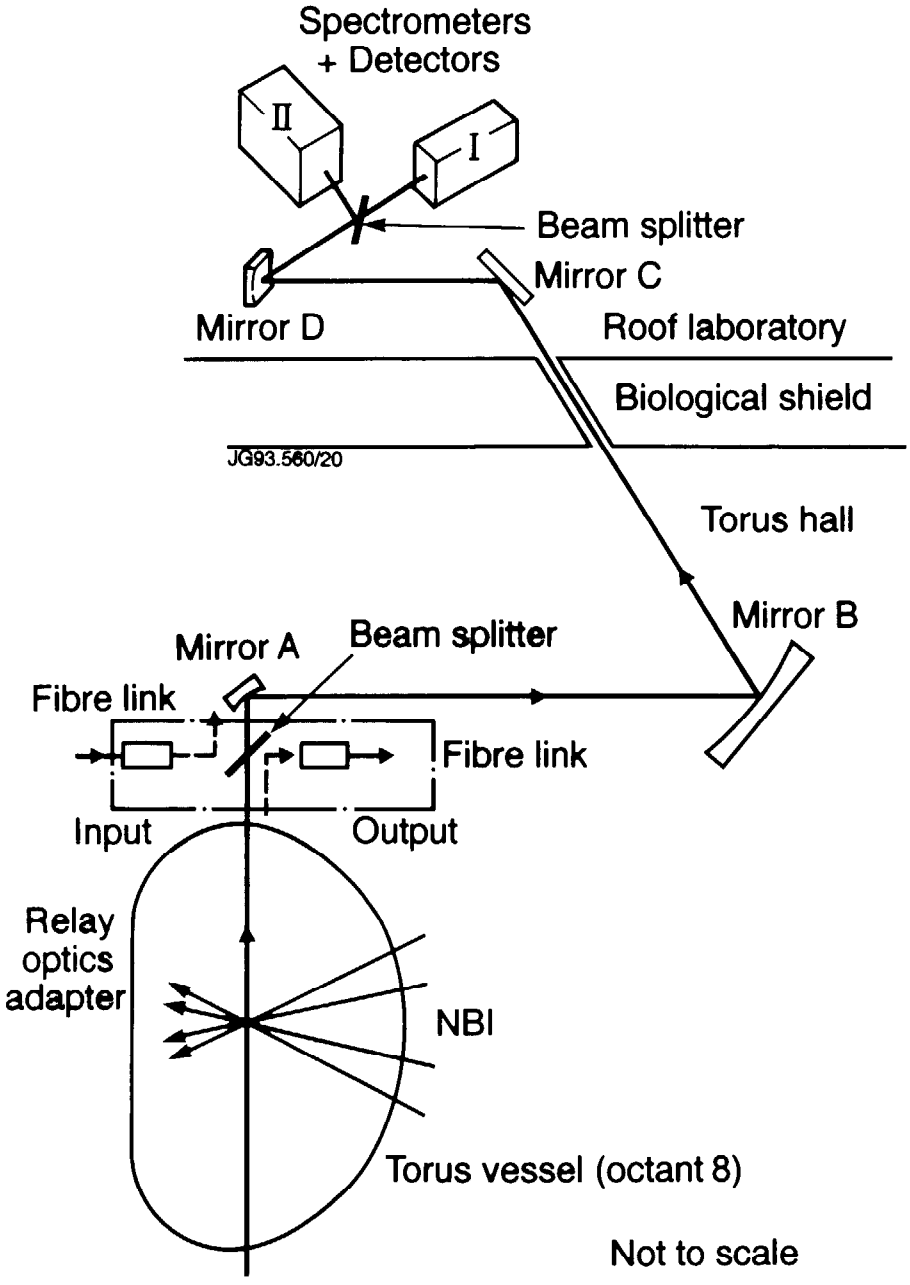

Fig.1: Overall schematic diagram of the diagnostic. Only the components needed for the collection of plasma light are shown. The beam splitter inserted above the observation port allows the simultaneous use of the port by a standard quartz-fibre link (output) and also the introduction of a calibration lamp into the direct-link light path (input).

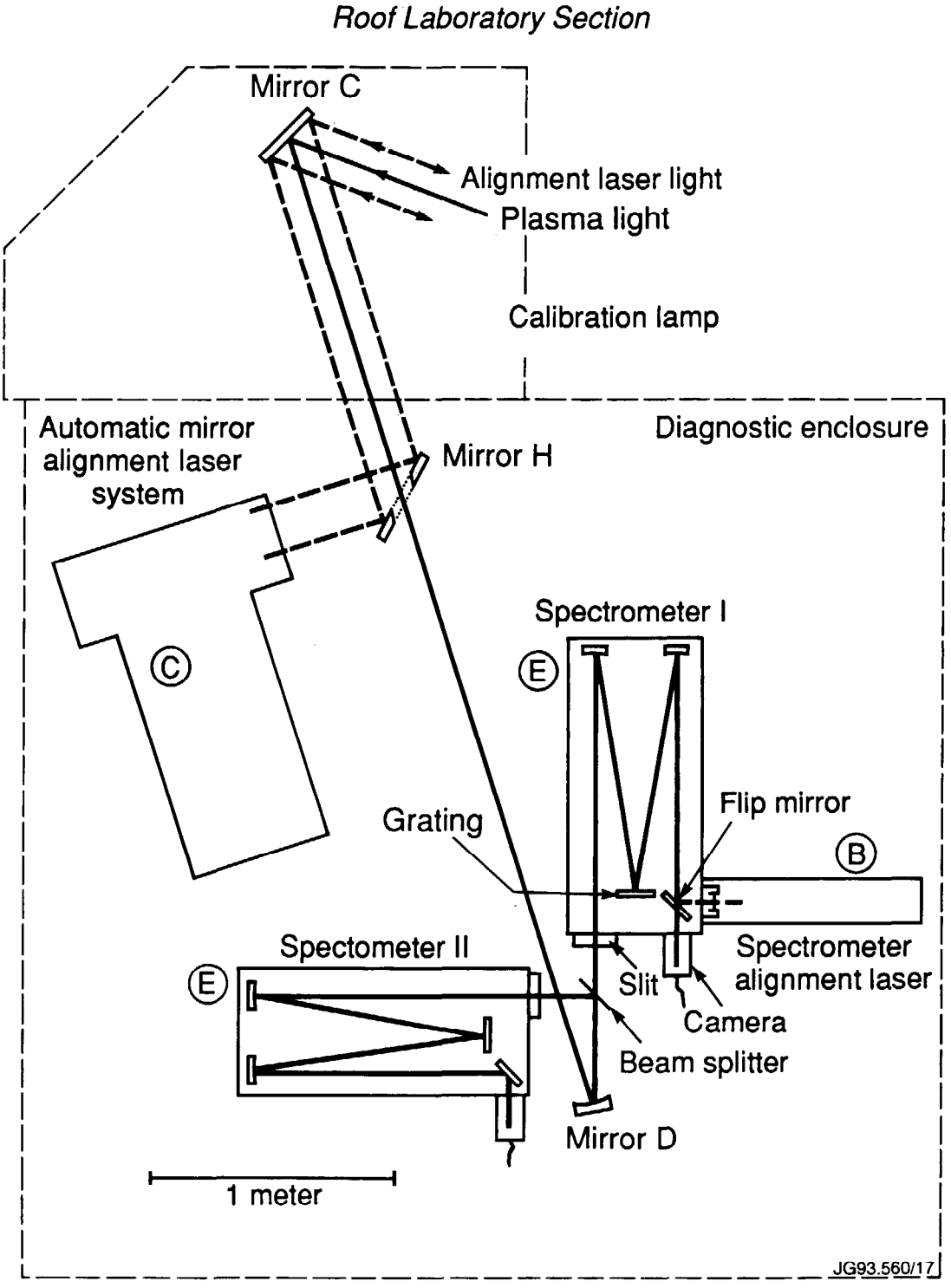

Fig.2: Schematic view of spectrometers located located beyond the biological shield in the roof laboratory on top of the JET torus hall. The second (dahed lines) spectrometer is presently commissioned for a simultaneous collection of UV and visible spectra using a bandpass filter as beam-splitter.

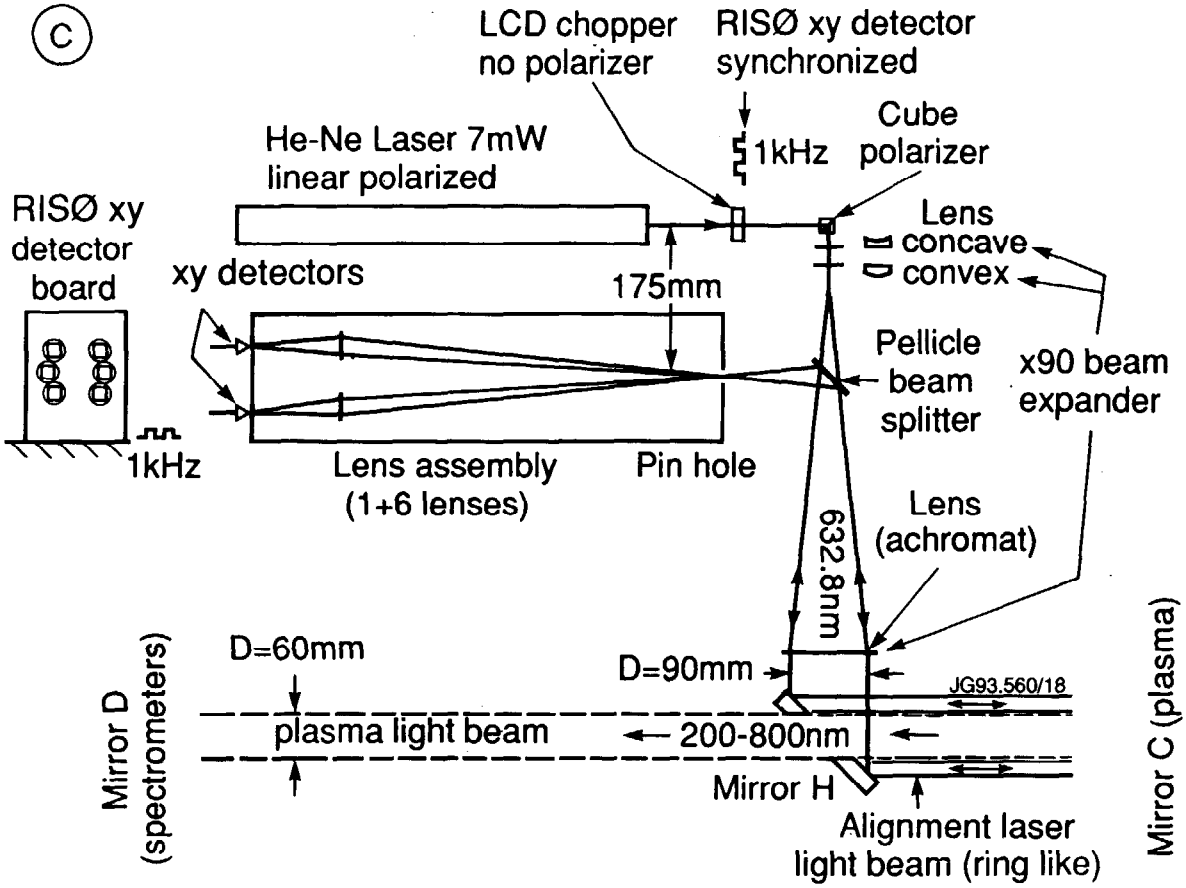

Fig.3: Schematic diagram of the alignment system, which uses the same optical path.

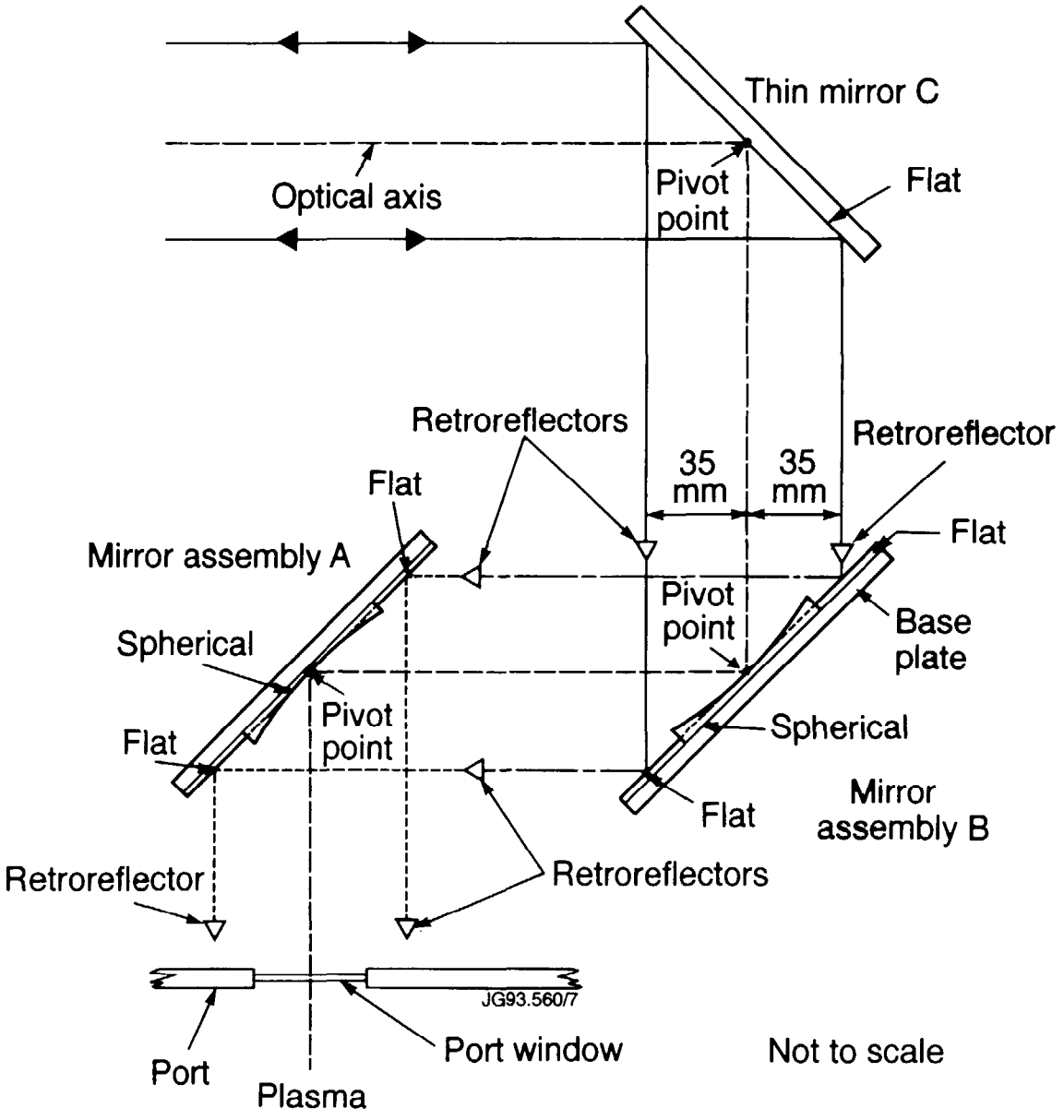

Fig.4: Schematic diagram of the alignment principle.

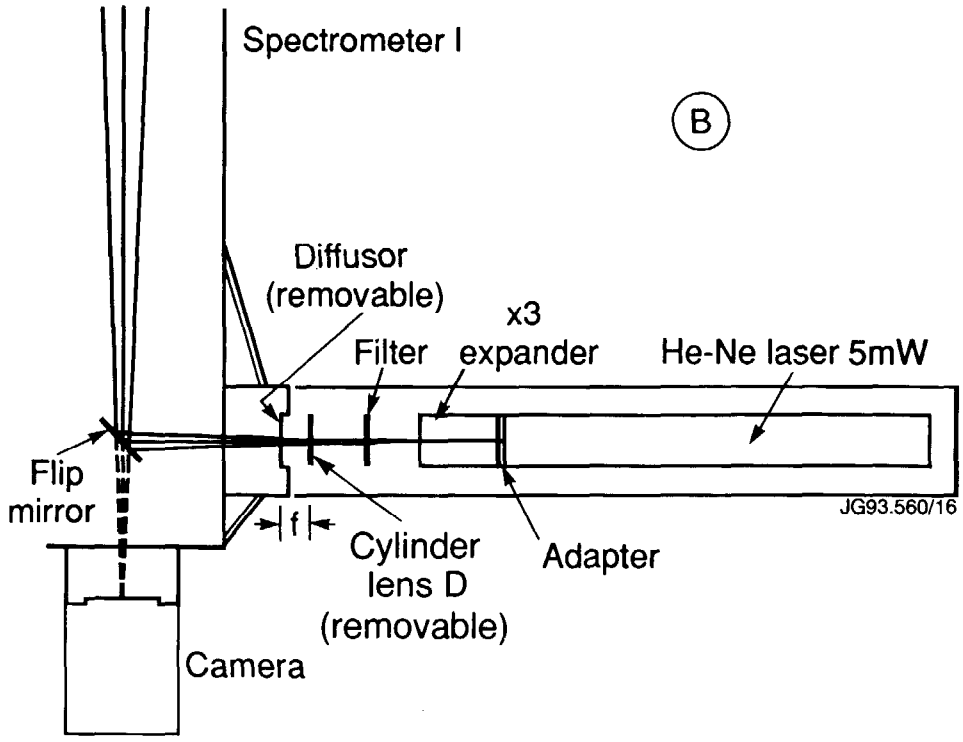

Fig.5: Spectrometer alignment laser which is used a) for the definition of the optical axis of the entire system and also the location of the calibration source close to the torus port, b) for the illumination of a diffuser at the exit slit which enables an assessment of the imaging properties along the light path.

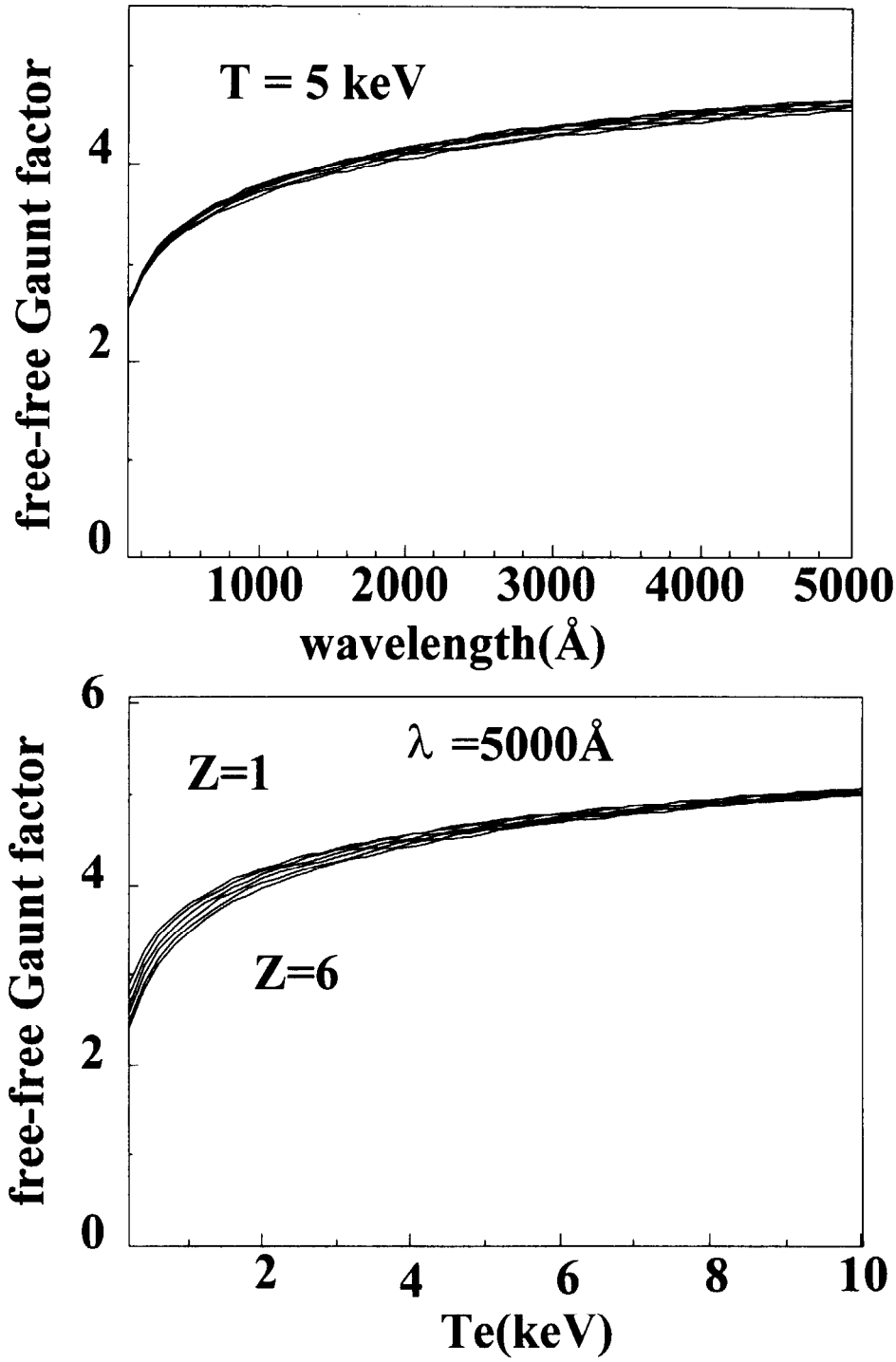

Fig.6: a) Free-free Gaunt factor versus wavelength at T_e=5keV, b) at γ=5000Å versus electron temperature.

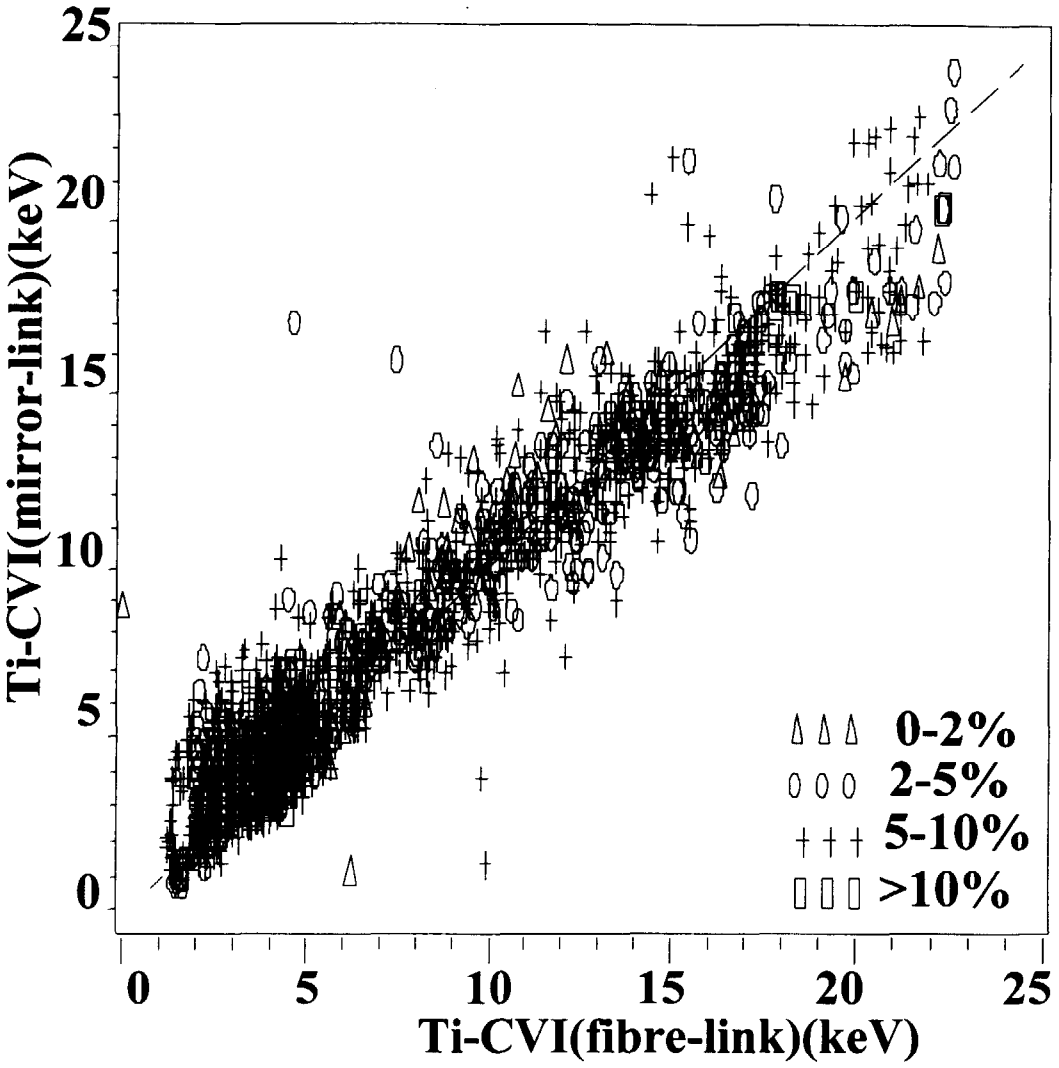

Fig.7: Overview of ion temperature measurements using the remote optical link and standard fibre link as deduced from the CVI CX spectrum

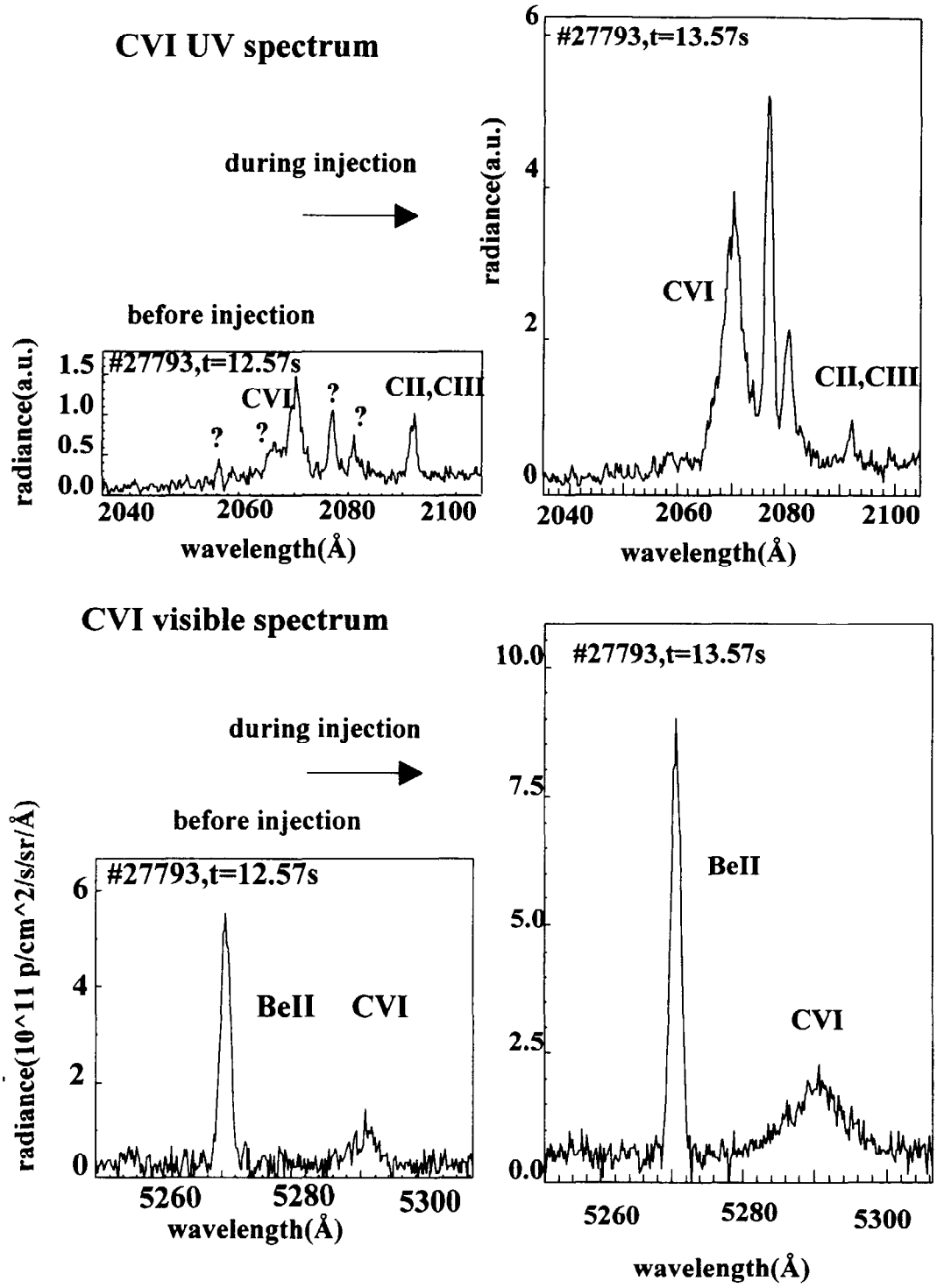

Fig.8: UV CX spectrum of CVI (n=6→n=5, γ=2070.3Å), JET pulse # 27793 at t = 13.57s. A second CX transition CVI(n=8→n=6, γ=2082.0Å) has a significantly lower emission rate. For comparison a CVI(8→7) spectra at the same times slices. Carbon concentration $n_c/n_e=0.075$, $n_c=3.510^{18}m^{-3}$.

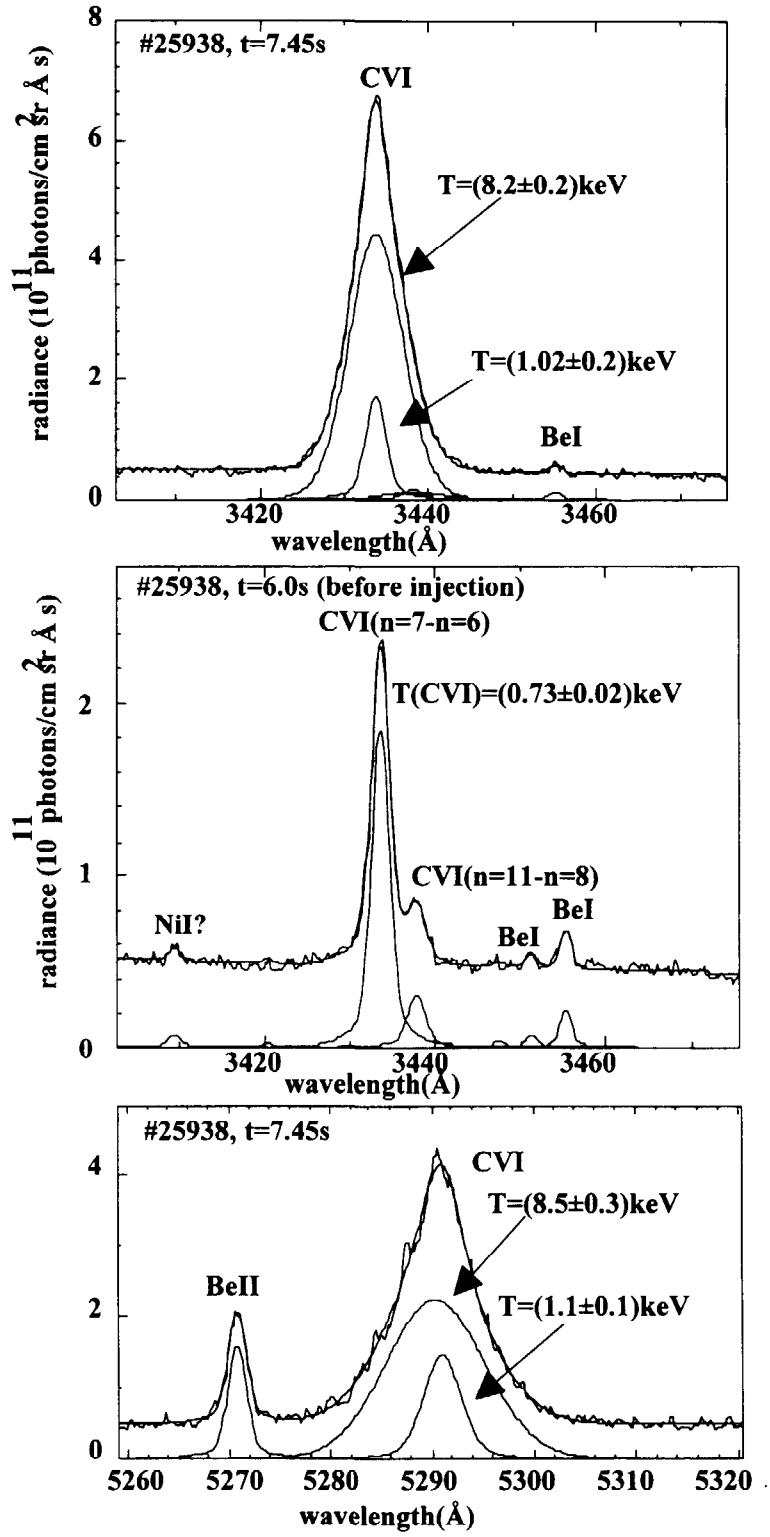

Fig.9 The UV CX spectrum CVI(n=7→n=6, =3433.7Å), JET pulse #25938, a) before start of neutral beam injection at t=6.5s and b) during injection at t=7.45s. The passive spectrum before injection shows the presence of a second CVI spectrum (n=11→n=8, at γ=3437.85Å) and a passive edge line attributed to BeI. c) For comparison a simultaneously measured visible CVI spectrum (n=8→n=7, at γ =5290.5Å), which is described by one passive edge and one active CX component. Within error bars the same temperature values are derived.

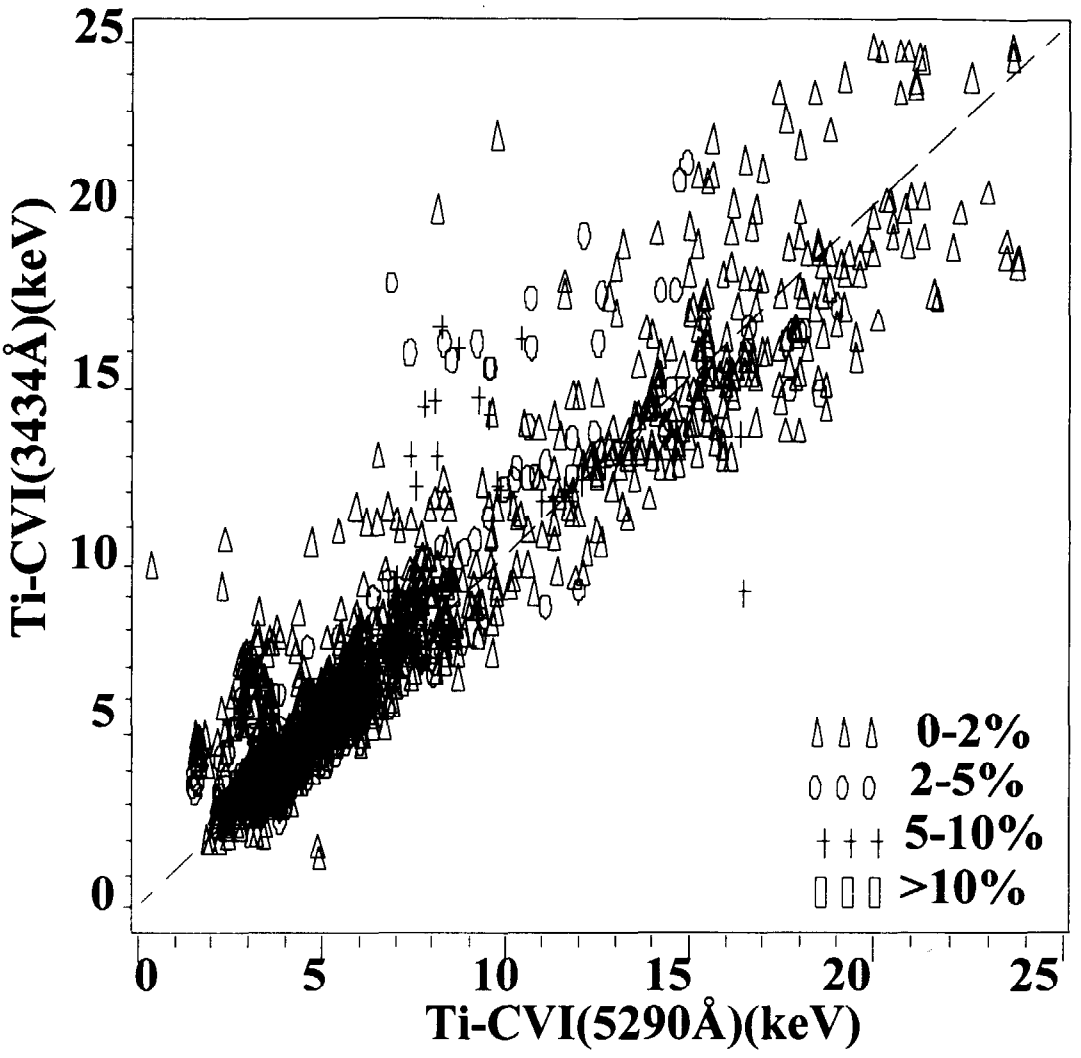

Fig.10: Overview of simultaneously measured central ion temperatures $T_i(0)$ derived from either the UV CX line CVI (n=7→n=6) at 3433.7Å or the visible CX line CVI (n=8→n=7) at 5290.5Å. The 1295 data points cover a pulse range between #25927 and #26136. A fixed amplitude ratio has been assumed for both the CX and edge CVI lines. The selected pulses represent an even mixture of 40 and 70 keV/amu beams. Different symbols reflect concentration levels of C^{6+}.

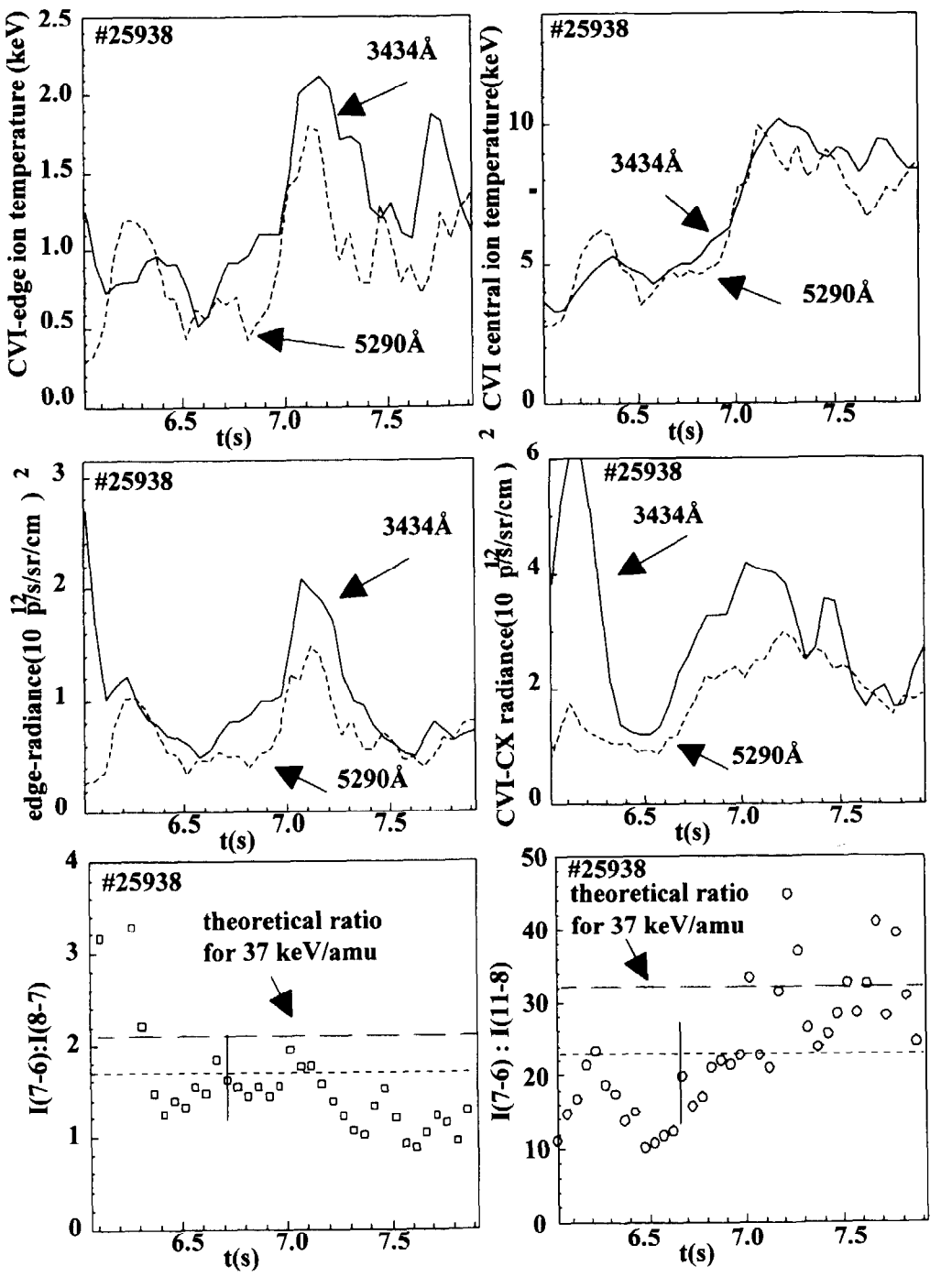

Fig.11: a) Measured CX intensity ratios CVI (n=7→n=6) and CVI (n=11→8) versus time and comparison with predicted ratio of effective emission rates (#25938). b)Time evolution of intensity ratio of edge components of the same transitions. c) Time evolution of intensity ratio of CX components.

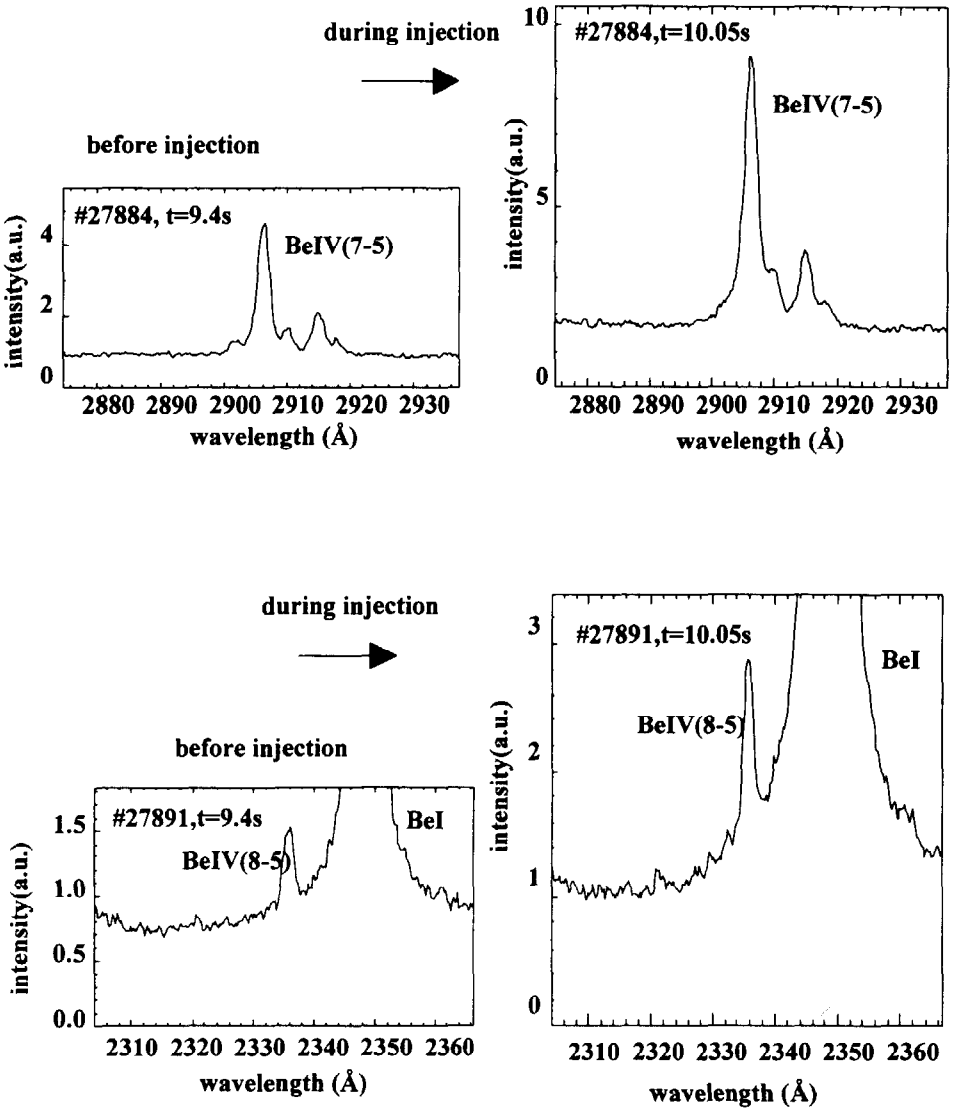

Fig.12: Low intensity UV CX transitions of BeIV a) #27891, n=3, n=8→5, γ=2335.9Å. The line is close to the intense BeI line at 2348.61Å, which excludes a useful CX analysis. b) A n=2, (n=7→5, γ=2906.2Å) BeIV transition with several additional edge lines.

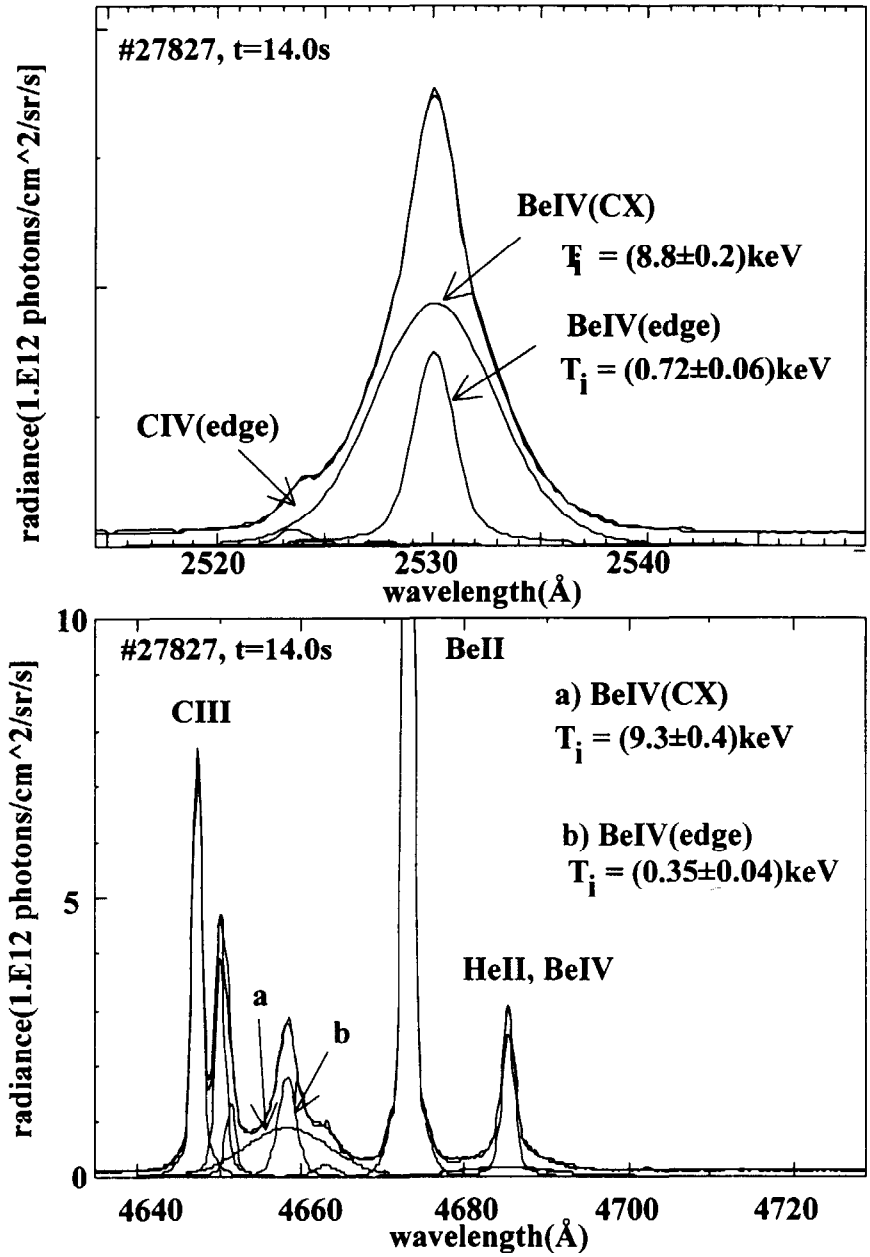

Fig.13: a) The dominant BeIV UV CX spectrum (n=1 transition, n=5→4,= 2530.5Å). In the same spectrum a CIV multiplet at 2523.7Å and a CII multiplet at 2538.98Å can be identified. The beryllium concentration at t=14.0s is $n_{Be}/n_e=0.01$ and its density $n_{Be}=2\cdot10^{17}m^{-3}$. b) The visible transitions BeIV(n=6→5, γ =4658.5Å) and BeIV(n = 8→6, γ = 4685.2Å) at the same time during JET pulse #27827 for direct comparison.

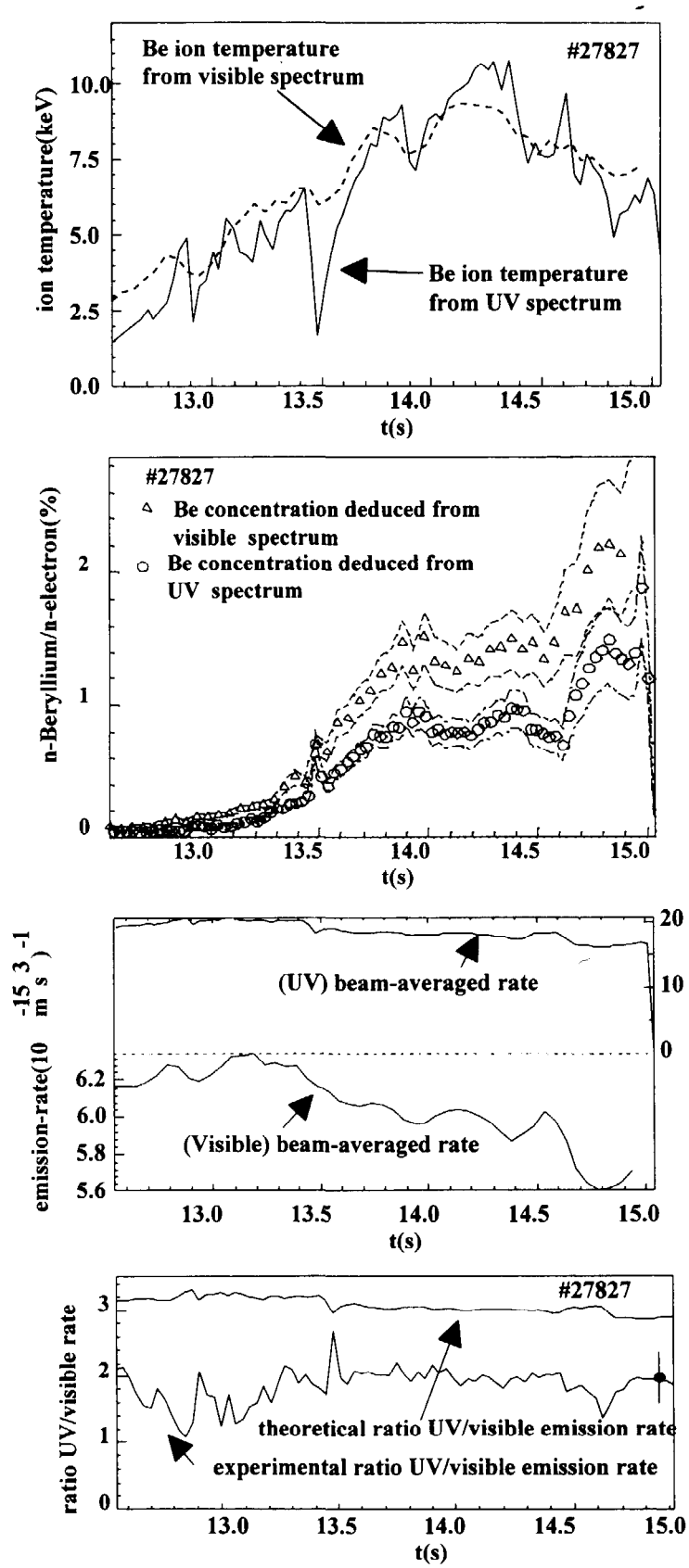

Fig.14: a) Central ion temperatures $T_i(0)$ derived from the UV-CX BeIV(5→4) spectrum at γ=2530.5Å and visible CX transition BeIV(6→5) at γ = 4658.25Å respectively (#27827). Note, that the temperature values from the visible spectrum are gained by a fit-procedure which couples the temperature of BeIV and HeII. b) Beryllium concentrations deduced from UV and visible CX intensities. The absolute intensities of the UV spectra are cross-calibrated via their bremsstrahlung level. c) Beam energy averaged UV and visible emission rates. d) Theoretical and experimental ratio of beam averaged rates.

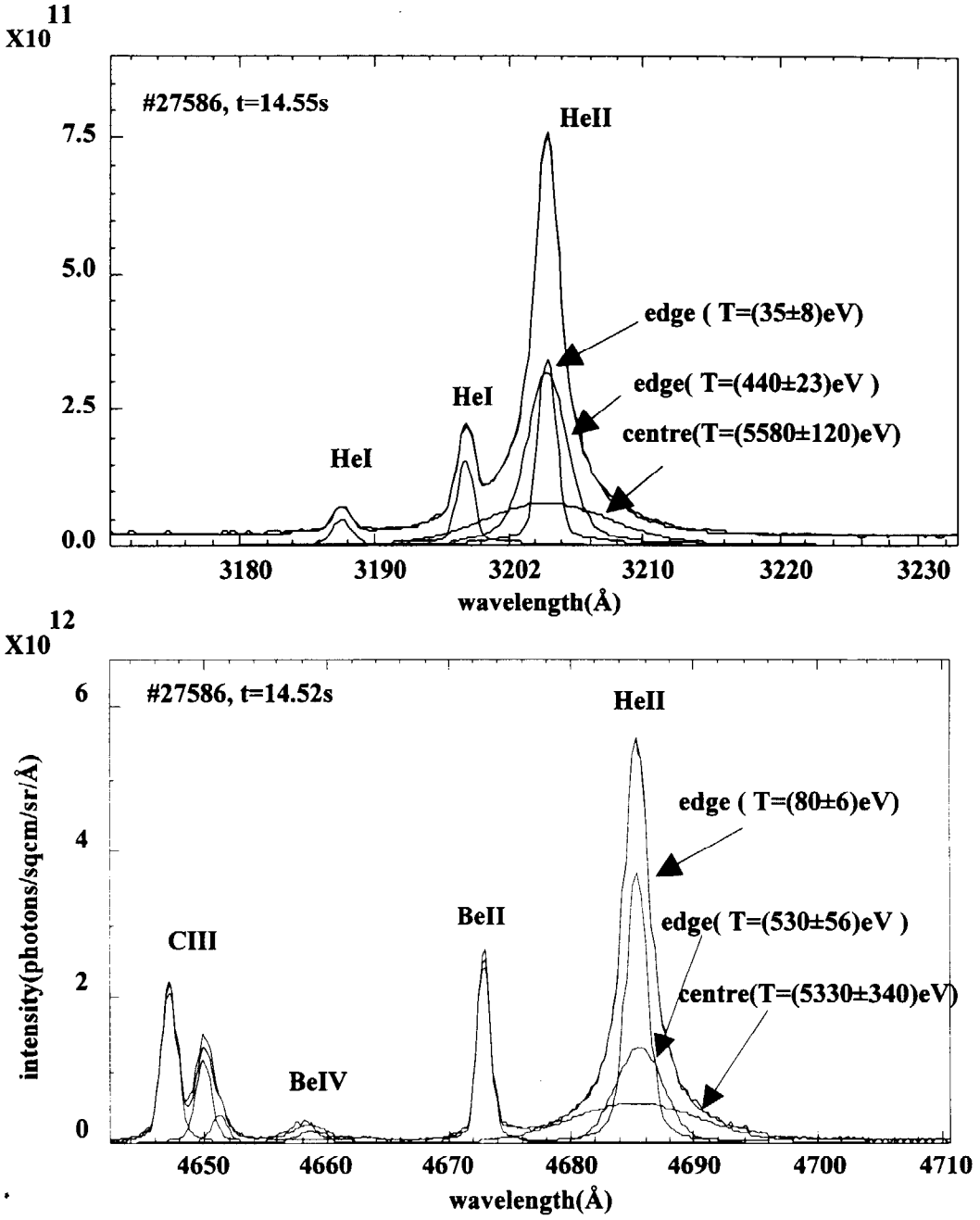

Fig.15: UV and visible CX HeII spectra in an almost pure 'helium' plasma (n_{He}/n_e>0.38, n_C/n_e≈0.017, n_{Be}/n_e≈0.023) JET pulse #27586. a) UV (n=5→3, γ= 3202.8Å) HeII spectrum with its two passive (electron impact and charge exchange) edge components and the active CX component representing the plasma centre. Two HeI edge lines are at 3186.74Å and 3196.74Å, b) Visible (n=4→3, γ= 4685.25Å) HeII spectrum and its neighbouring BeIV spectrum.

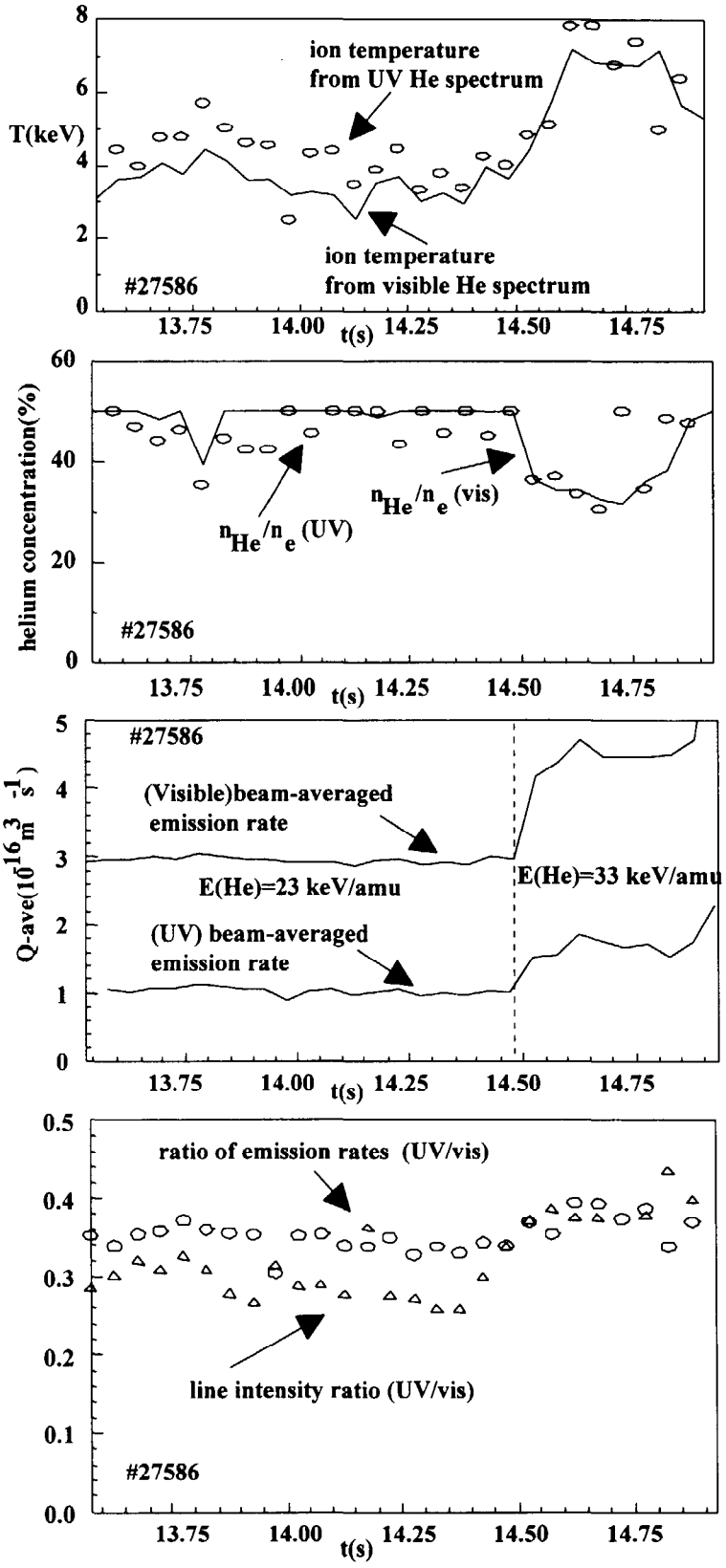

Fig.16: a) Ion temperatures derived from UV-CX line HeII (n=2,n=5→3) at 3202.8Å and comparison with values derived the visible CX line HeII (n=1, n=4→3) at γ = 4685.25Å. b) helium concentrations derived from UV and visible spectrum. c) Beam-averaged rates, d) Ratio of beam averaged rates derived from photon fluxes and theoretical values. Note that the beams are $^3He^0$ beams with one full energy component, but two combinations banks of beam energies (23 and 44 keV/amu) which are switched on at different times.

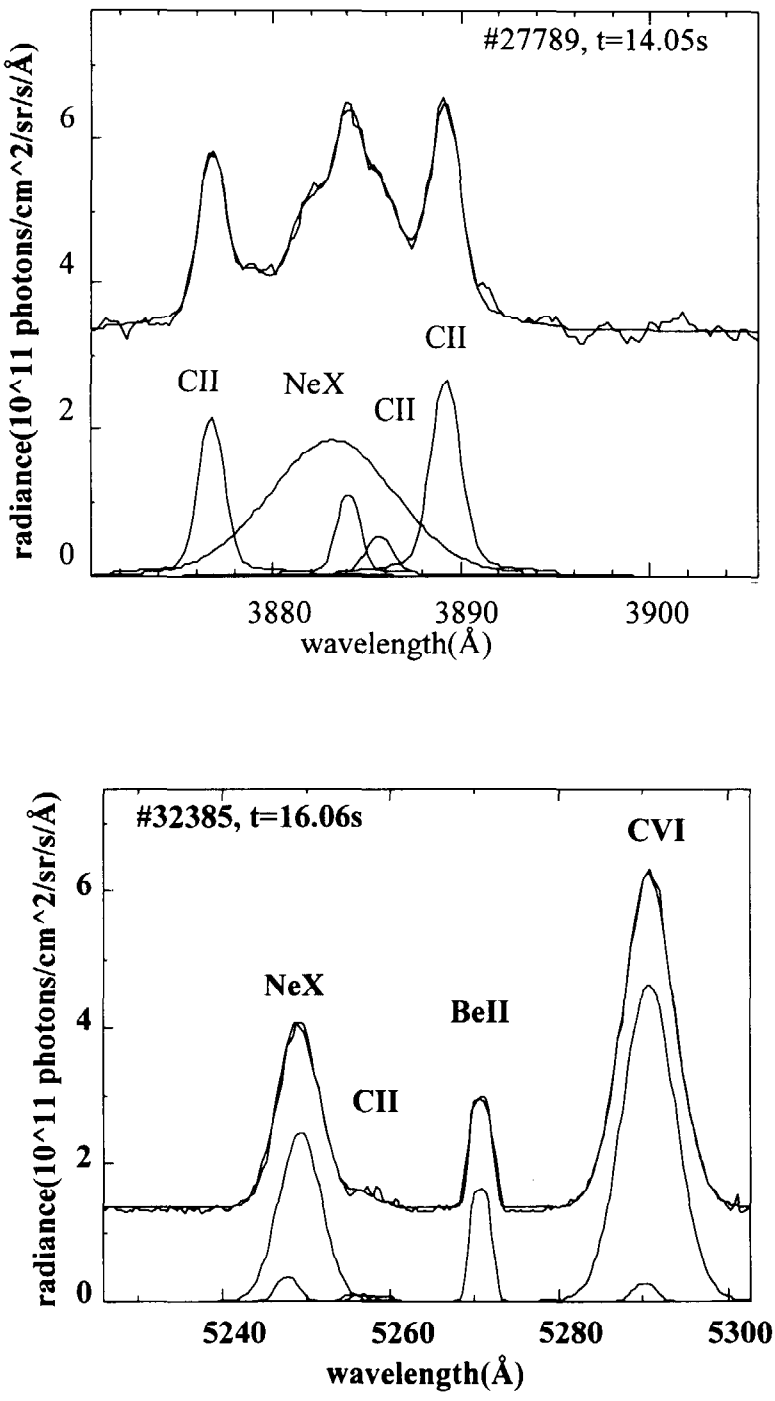

Fig.17: a) UV CX spectrum of NeX(n=10→9 at =3884.0Å) showing several CII and CIII edge multiplets lines in the same spectral range. The dominant CII multiplets are approximated by single Gaussian shapes. b) Twin spectrum in the visible wavelength range, NeX(n=11→10 at =5248.70Å), however at a different pulse number (#32385). The CII and CIII multiplets present in the visible wavelength NeX spectrum at 5249.11Å and 5279.71Å respectively. The Ne^{10+} concentration is 2.3%.